Monthly Notices of the ROYAL ASTRONOMICAL SOCIETY

MNRAS **513,** 822–834 (2022) https://doi.org/10.1093/mnras/stac814
Advance Access publication 2022 March 24

Probing the parameters of the intergalactic medium using quasars

Tony Dalton,[1]★ Simon L. Morris ,[1] Michele Fumagalli [2,3] and Efrain Gatuzz[4]

[1]*Centre for Extragalactic Astronomy, Durham University, South Road, Durham DH1 3LE, UK*
[2]*Dipartimento di Fisica 'G. Occhialini', Università degli Studi di Milano-Bicocca, Piazza della Scienza 3, I-20126 Milano, Italy*
[3]*INAF - Osservatorio Astronomico di Trieste, via G. B. Tiepolo 11, I-34143 Trieste, Italy*
[4]*Max-Planck-Institut für extraterrestrische Physik, Gießenbachstraße 1, D-85748 Garching, Germany*

Accepted 2022 March 18. Received 2022 March 17; in original form 2022 January 28

ABSTRACT

We continue our series of papers on intergalactic medium (IGM) tracers using quasi-stellar objects (QSOs), having examined gamma-ray bursts (GRBs) and blazars in earlier studies. We have estimated the IGM properties of hydrogen column density ($N_{\rm HXIGM}$), temperature, and metallicity using *XMM–Newton* QSO spectra over a large redshift range, with a collisional ionization equilibrium model for the ionized plasma. The $N_{\rm HXIGM}$ parameter results were robust with respect to intrinsic power laws, spectral counts, reflection hump, and soft excess features. There is scope for a luminosity bias given both luminosity and $N_{\rm HXIGM}$ scale with redshift, but we find this unlikely given the consistent IGM parameter results across the other tracer types reviewed. The impact of intervening high-column density absorbers was found to be minimal. The $N_{\rm HXIGM}$ from the QSO sample scales as $(1 + z)^{1.5 \pm 0.2}$. The mean hydrogen density at $z = 0$ is $n_0 = (2.8 \pm 0.3) \times 10^{-7}$ cm^{-3}, the mean IGM temperature over the full redshift range is $\log(T/{\rm K}) = 6.5 \pm 0.1$, and the mean metallicity is $[X/{\rm H}] = -1.3 \pm 0.1 (Z \sim 0.05)$. Aggregating with our previous GRB and blazar tracers, we conclude that we have provided evidence of the IGM contributing substantially and consistently to the total X-ray absorption seen in the spectra. These results are based on the necessarily simplistic slab model used for the IGM, due to the inability of current X-ray data to constrain the IGM redshift distribution.

Key words: galaxies: high-redshift – intergalactic medium – quasars: general – gamma-ray burst: general – X-rays: general.

1 INTRODUCTION

Most baryonic matter in the intergalactic medium (IGM) is not in the form of luminous virialized matter (Shull, Smith & Danforth 2012), and the majority of hydrogen and helium is ionized. In order to measure the IGM density, metallicity, and temperature, the observation of metals is essential. Powerful cosmological sources such as gamma-ray bursts (GRBs), blazars, and quasi-stellar objects (QSOs) are currently the most effective targets to study the IGM out to high redshift as their X-ray absorption provides information on the total absorbing column density of the matter, subject to the IGM model chosen and assumptions.

QSOs are an extremely luminous form of active galactic nuclei (AGNs) observed over a huge cosmological range with the current most distant being J0313−1806 at redshift $z = 7.642$ (Wang et al. 2020). Under the generally accepted scenario, ultraviolet (UV) emission in QSOs is produced by viscous dissipation in the accretion disc where the gravitational energy of the infalling material is partially transformed into radiation (Shakura & Sunyaev 1973). The UV photons are Comptonized to X-rays by a corona of hot relativistic electrons around the accretion disc (Haardt & Maraschi 1993). These X-rays can illuminate the accretion disc, being reflected back towards the observer. The observational signs of such reflection features are iron emission lines, Fe K absorption edge, and Compton scattering hump. However, these are not always apparent or observed. While features such as the Compton hump, soft excess, and iron emission lines are frequently observed in lower luminosity AGN, particularly at lower redshift, they are not often observed in QSOs where the very powerful emission continuum dominates (Scott et al. 2011 and references therein). QSOs have been extensively studied for many decades across a very wide band of frequencies from radio to X-ray. The availability of UV data bases and catalogues enables broad-band comparison with X-rays for our purposes. The clear non-linear relation between the UV and X-ray components has been measured in detail, and noted to be reasonably constant over redshift and luminosity ranges (e.g. Risaliti & Lusso 2019; Salvestrini et al. 2019; Lusso et al. 2020 and references therein). The very consistent spectra of QSOs observed over an extensive redshift range make them attractive as IGM tracers, as it can then be hypothesized that deficits or hardening in continuum curvature that are related to redshift could be interpreted as signatures of IGM absorption.

QSOs as X-ray tracers of the IGM have been well studied in the past (e.g. Wilkes & Elvis 1987; Elvis et al. 1994b; Page et al. 2005; Behar et al. 2011; Starling et al. 2013). X-ray absorption is typically dominated by metal ions and reported as an equivalent hydrogen column density ($N_{\rm HX}$). The early observations of excess absorption in QSOs at high redshift in X-ray over the known Galactic absorption ($N_{\rm HXGAL}$) were unexpected, as in X-ray, the absorbing cross-section decreases as the observed spectral energy increases with redshift (e.g. Elvis et al. 1994b; Cappi et al. 1997; Elvis et al. 1998; Fiore et al. 1998). This excess absorption was initially assumed to be located in the QSO host. Reeves & Turner (2000) were among

★ E-mail: tonydalton@live.ie

© 2022 The Author(s)
Published by Oxford University Press on behalf of Royal Astronomical Society

Downloaded from https://academic.oup.com/mnras/article/513/1/822/6553838 by Durham University user on 28 June 2022

the first to strongly advocate a relation between excess absorption and redshift but noted that the assumption of all such excess being at the QSO rest frame could lead to overestimation of column densities as the absorbing material could lie anywhere on the line of sight (LOS). Later studies explored the possibility of the IGM contributing to the excess absorption and found it to be related to redshift (e.g. Eitan & Behar 2013; Starling et al. 2013; Arcodia et al. 2018). However, all such studies assumed by convention that the absorbers were neutral and at solar metallicity. As typical QSO hosts, and IGM absorbers are partially ionized and have low metallicity, the resulting reported column densities are, therefore, lower limits. In our previous studies on GRBs (Dalton & Morris 2020; Dalton, Morris & Fumagalli 2021a, hereafter D20 and D21a) and blazars (Dalton et al. 2021b, hereafter D21b), we used realistic parameter ranges for metallicity and temperature in collisional ionization absorption models for the IGM. We found strong evidence for IGM X-ray mean column density rising with redshift in the spectra of both GRBs and blazars. We now continue the series using similar IGM and continuum models to study QSO spectra. In this paper, all data are taken from the European Space Agency's *XMM−Newton* Photon Imaging Camera (EPIC; Strüder et al. 2001) which has reasonable response down to 0.15 keV, high sensitivity to extended emission, and large effective area enabling detailed analysis of soft X-ray properties. *XMM−Newton* has three cameras, PN, MOS-1, and MOS-2. Our data are taken from PN except for our highest redshift QSOs where we included the MOS-1 and MOS-2 data to increase spectral counts.

In our previous papers in this series, we studied GRBs and blazars as tracers of IGM properties and possible variation with redshift (D20, D21a, and D21b). We continue the series in this paper with the study of QSOs. Our main objective is to estimate the IGM column density, temperature, and metallicity, using an ionized absorption model, on the LOS to QSOs. Our continuing hypothesis is that the integrated IGM column density from IGM absorption increases with redshift. We analyse this highly ionized IGM absorption in addition to examining appropriate host environment and continuum intrinsic models. We test the robustness of our results and aggregate our QSO sample with our GRB and blazar samples for cross-tracer comparison.

The sections that follow are: Section 2 describes the data selection and methodology; Section 3 covers the models for the IGM LOS including assumptions and parameters, and QSO continuum models; Section 4 gives the results of QSO spectra fits using collisional IGM models with free IGM key parameters; in Section 5 we test the robustness of the IGM model fits including a review of the QSO UV spectra for any high-density absorbers; in Section 6 we aggregate GRB and blazar samples with our QSO sample for cross-tracer analysis. In Section 7, we discuss and compare results with other studies and Section 8 gives conclusions. We suggest readers interested in the IGM property results see Sections 4, 6, and 8. For spectra fitting methodology and model assumptions readers should also go to Sections 2 and 3. Finally, for more detailed examination of robustness of the QSO spectra fitting and discussion on other studies, read Sections 5 and 7. In this paper where relevant, we adopt the cosmological parameters $\Omega_M = 0.3$, $\Omega_\Lambda = 0.7$, and $H_0 = 70\ \mathrm{km\ s^{-1}\ Mpc^{-1}}$.

2 DATA SELECTION AND METHODOLOGY

Our sample of QSOs is taken from the catalogue created by Lusso et al. (2020) based on the 14th Data Release of the *Sloan Digital Sky Survey* (SDSS-DR14) (York et al. 2000) which they cross-matched with 4*XMM–Newton* Data Release-9 (4*XMM–Newton*-DR9) data giving an initial sample of 24 947 QSOs. We applied an initial minimum threshold of X-ray counts >500 for the PN camera to ensure high signal-to-noise spectra. As the number of QSOs with $z > 4$ decreases dramatically, we drew from samples in Page et al. (2005), Grupe et al. (2006), Eitan & Behar (2013), Nanni et al. (2017), Vito et al. (2019), and Medvedev et al. (2021). For $z < 4$ QSOs, we selected those with highest counts, maintaining a redshift spread. We relaxed our minimum count cut-off requirement slightly above redshift $z \sim 3.8$, with three QSOs have counts between 400 and 500. The highest two redshift QSOs have data from all three EPIC cameras to increase the spectral counts. Our final sample of 48 QSOs has a redshift range of $0.114 \leq z \leq 6.18$ (Table 1).

Radio loudness (R) is typically defined as the ratio of the flux densities at rest frame 5 GHz and 4400 Å, with $R \geq 10$ and $R < 10$ for radio-loud (RLQ) and radio-quiet (RQQ), respectively (Kellermann et al. 1989). We include both RLQ and RQQ in our sample but exclude broad-absorption line QSOs as these are known to be highly absorbed in X-ray and could dominate any possible IGM absorption. In general, for a given optical luminosity, the X-ray emission from RLQs is about three times greater than that from RQQs which allows them to be studied out to higher redshifts (Scott et al. 2011 and references therein). As a result, 19 out of our 48 QSOs are RLQ which may be a source of bias given on average, approximately 10 per cent of QSOs are RLQ (e.g. Grupe et al. 2006). We explore this in Section 5.

The *XMM–Newton* EPIC spectra were obtained in timing mode and reduced with the Science Analysis System (SAS2, version 19.1.0). First, we processed each observation with the EPCHAIN SAS tool. We used only single-pixel events (PATTERN==0) while bad time intervals were filtered out for large flares applying a 1.0 counts $\mathrm{s^{-1}}$ threshold. In order to avoid bad pixels and regions close to CCD edges, we filtered the data using FLAG==0. We manually inspected the source and background subtraction region for each observation.

For our fitting, we use XSPEC version 12.11.1 (Arnaud 1996). We use the C-statistic (Cstat; Cash 1979) which is based on the Poisson likelihood and gives more reliable results for small number counts per bin. As we are using total X-ray spectral absorption for the IGM, we can expect some degeneracy between the parameters. We, therefore, follow the same method as in our other papers in this series (D21a and D21b) using both STEPPAR function and Markov chain Monte Carlo to overcome the problem of local probability maxima, and to give confidence intervals on our IGM property results. We adopt the approach that a reduction of Cstat>2.71, >4.6, and >6.25 for one, two, and three additional interesting parameters corresponds to 90 per cent significance (Reeves & Turner 2000; Ricci et al. 2017). To avoid empty channels, we binned spectra to have a minimum count of one count per bin so the Cstat value is independent of the count numbers (Nanni et al. 2017). We assume a homogeneous isotropic IGM as all our QSO sample has LOS much greater than the large-scale structure, while acknowledging that large individual absorbers can still impact the LOS (tested in Section 5).

3 MODELS FOR THE QSO CONTINUUM AND LOS FEATURES

In this section, we describe our IGM models and parameter ranges, the models used for fitting the intrinsic spectra, absorption of the QSOs, and our Galaxy. We emphasize that we are not attempting to find a model fully consistent with the QSO spectrum, so long as our intrinsic model sufficiently represents spectral curvature and shape, with the remaining spectral features being attributable to the

Downloaded from https://academic.oup.com/mnras/article/513/1/822/6553838 by Durham University user on 28 June 2022

Table 1. SDSS-DR14 and 4*XMM–Newton*-DR9 cross-correlation QSO sample. For each QSO, the columns give the name, radio type (RLQ, RQQ, or unknown), redshift, number of counts in 0.3–10 keV range, count rate (s^{-1}), Galactic column density ($\log(N_{\rm HXGAL}/cm^{-2})$), and unabsorbed luminosity (2–10 keV) ($\log(L/erg\,s^{-1})$). Co-added spectra for a number of QSOs are used, often observed over a period of time, so we do not provide individual observation information.

QSO	Radio type	z	Total counts	Mean count rate (s^{-1})	log ($N_{\rm HXGAL}/cm^{-2}$)	log (L/erg s^{-1})
J142952+544717[a]	RLQ	6.18	725	0.046	20.18	46.36
022112.62−034252.2[a]	Unknown	5.01	339	0.034	20.30	45.14
001115.23+144601.8	RLQ	4.96	2258	0.096	20.31	46.47
143023.73+420436.5	RLQ	4.71	13162	0.157	20.29	47.11
223953.6−055220.0	RQQ	4.56	450	0.015	20.58	45.63
151002.93+570243.3	RLQ	4.31	1395	0.15	20.17	45.88
133529.45+410125.9	RQQ	4.26	626	0.055	19.98	46.09
132611.84+074358.3	RQQ	4.12	947	0.025	20.48	46.09
163950.52+434003.7	RLQ	3.99	1158	0.029	20.30	45.76
021429.29−051744.8	RLQ	3.98	1126	0.018	20.30	45.57
133223.26+503431.3	RQQ	3.81	404	0.022	20.03	45.60
200324.1−325144.0	RLQ	3.78	3484	0.23	20.86	46.56
200324.1−135245.1	RLQ	3.77	2963	0.21	20.90	45.86
122135.6+280614.0	RLQ	3.31	2994	0.093	20.30	45.35
042214.8−384453.0	RLQ	3.11	1840	0.22	20.31	45.48
083910.89+200207.3	RLQ	3.03	4251	0.103	20.3	45.86
111038.64+483115.6	RQQ	2.96	741	0.022	20.10	45.35
122307.52+103448.2	RQQ	2.75	535	0.029	20.35	45.48
115005.36+013850.7	Unknown	2.33	954	0.014	20.36	45.19
121423.02+024252.8	RLQ	2.22	5394	0.077	20.25	45.62
112338.14+052038.5	RLQ	2.18	826	0.031	20.64	45.62
123527.36+392824.0	RQQ	2.16	553	0.017	20.17	45.07
134740.99+581242.2	RLQ	2.05	2978	0.112	20.11	45.66
095834.04+024427.1	RQQ	1.89	1444	0.023	20.44	44.87
093359.34+551550.7	RQQ	1.86	2309	0.09	20.26	45.64
133526.73+405957.5	RQQ	1.77	634	0.062	19.97	45.39
100434.91+411242.8	RQQ	1.74	9558	0.27	20.05	45.90
104039.54+061521.5	RLQ	1.58	946	0.019	20.45	44.94
083205.95+524359.3	RQQ	1.57	1303	0.016	20.58	44.61
112320.73+013747.4	RQQ	1.47	1801	0.078	20.62	45.37
091301.03+525928.9	RQQ	1.38	1221	0.44	20.20	45.88
121426.52+140258.9	RLQ	1.28	946	0.019	20.44	45.19
105316.75+573550.8	RQQ	1.21	2059	0.066	19.75	45.12
085808.91+274522.7	RQQ	1.09	3158	0.043	20.49	44.71
095857.34+021314.5	RQQ	1.02	1904	0.77	20.43	45.10
125849.83−014303.3	RQQ	0.97	7032	0.20	20.20	45.09
082257.55+404149.7	RLQ	0.86	815	0.158	20.65	44.96
150431.30+474151.2	RQQ	0.82	1499	0.106	20.34	45.02
111606.97+423645.4	RQQ	0.67	2409	0.081	20.25	44.57
130028.53+283010.1	RLQ	0.65	6859	0.314	19.97	45.03
111135.76+482945.3	RQQ	0.56	4081	0.150	20.10	44.67
091029.03+542719.0	RQQ	0.53	2073	0.058	29.32	44.16
105224.94+441505.2	RQQ	0.44	1237	0.156	20.05	44.19
223607.68+134355.3	RQQ	0.33	3106	0.058	20.68	44.30
144645.93+403505.7	RQQ	0.27	15843	0.959	20.10	44.14
123054.11+110011.2	RQQ	0.24	6368	1.158	20.33	44.33
103059.09+310255.8	RLQ	0.18	37274	1.79	20.29	44.36
141700.81+445606.3	RQQ	0.11	29070	1.386	20.09	43.56

Note.
[a]These QSOs had poor high-energy spectra above 2 keV so the range taken was from 0.2 to 2.0 keV.

IGM. We, therefore, do not necessarily expect our modelling to yield any physical insight into the nature of the QSO engine itself. Given the moderate resolution of *XMM–Newton*, our spectral modelling and analysis pertains to the overall continuum absorption and not individual lines, edges or features (D21a and D21b).

3.1 Galactic absorption

We use TBABS (Wilms, Allen & McCray 2000, hereafter W00) with $N_{\rm HXGAL}$ fixed to the values based on Willingale et al. (2013) and Kalberla et al. (2005). We use W00 solar abundances which factor in H_2 and dust in the galaxy interstellar medium.

Downloaded from https://academic.oup.com/mnras/article/513/1/822/6553838 by Durham University user on 28 June 2022

3.2 Continuum models

In the energy range 0.3–10 keV, QSO spectra are typically modelled with a simple power law. Some studies add a high-energy cutoff at ∼100 keV or higher (e.g. Ricci et al. 2017), but such cut-off values are well outside our X-ray energy range. Many QSOs show curvature, particularly in soft X-ray and a log-parabolic power law can be more appropriate. A Compton reflection hump is a common feature in QSOs, mainly RQQ. However, the visibility of this component in the observed spectra of QSOs is low, as their emission is mainly dominated by the luminous continuum (e.g. Reeves & Turner 2000; Scott et al. 2011). In high-luminosity QSOs, the reflection component may be intrinsically weaker due to possible ionization of the inner accretion disc, reducing the neutral matter available to generate a reflection feature (Mushotzky, Done & Pounds 1993). There is little observational evidence, particularly for higher redshift QSOs ($z > 2$) of the iron emission line, probably due to the dominant emission continuum (Page et al. 2005). QSOs sometimes show a soft excess, particularly at lower redshifts. This was initially postulated to be the hard tail of the UV 'big blue bump'. While there is no consensus on the origin of the soft excess, there are now several prominent theories e.g. an artefact of ionized absorption (e.g. Gierliński & Done 2004), Comptonization of UV photons (e.g. Done et al. 2012), and relativistically blurred disc reflection (e.g. Crummy et al. 2006). As the soft excess rarely shows above redshift $z > 0.3$, and the reflection hump is also rarely seen in QSOs, we omit adding specific components for these features in our initial fitting.

Accordingly, we model the QSO continuum with a simple and a log-parabolic power law. In Section 5, we robustly explore whether the inclusion of model components for reflection and/or soft excess improves the fit and/or impacts any IGM absorption.

3.3 QSO host absorption

As noted in Section 1, by convention many X-ray QSO studies assume any absorption in excess of our Galaxy is due to the host galaxy, with the absorber assumed to be neutral and with solar metallicity. To more accurately isolate any absorption by the QSO host, we base our model on the findings in the Quasar Probing Quasar series (e.g. Hennawi et al. 2006; Prochaska & Hennawi 2009; Hennawi & Prochaska 2013; Prochaska et al. 2013). Accordingly, our host model assumes collisionally ionized absorption (CIE) in the circumgalactic medium (CGM) at fixed parameters of $\log(N_{\rm HX}/{\rm cm}^{-2}) = 20$, $\log({\rm T/K}) = 6$, and $[X/{\rm H}] = -1\,(Z/Z\odot = 0.1)$. We use the XSPEC CIE model HOTABS (Kallman et al. 2009). We note that there is evidence of metallicity evolution in QSOs (e.g. Prochaska et al. 2014 and references therein) but not sufficient to warrant leaving the metallicity parameter variable in the host model. Further, Damped Lyman Alpha Systems (DLAs) have been observed on the LOS to QSOs. However, their very low incidence means they have limited potential impact on most QSO spectra. We examine this further in Section 5. Finally, we note that the incidence of QSOs with significantly reddened optical spectra is rare, indicating that the dust/gas ratio is low (Page et al. 2005). Therefore, we assume there is no dust impact on the assumed host absorption. We note that our choice of QSO host model precludes any significant host X-ray absorption.

3.4 Ionized IGM component

We follow the D21a and D21b methodology for the modelling the IGM absorption. We initially fitted a subsample of QSOs with both photoionization equilibrium (PIE) and CIE, respectively, models separately to study these examples. Similar results for $N_{\rm HXIGM}$ were obtained for both models, consistent with D21a and D21b. Some combination of CIE and PIE absorption is the most physically plausible scenario for the full LOS. It is not possible to determine which ionization model is the better single model for the IGM at all redshifts, and we follow D21b, fitting with the CIE model HOTABS only. As noted in Section 3, we are modelling and fitting the overall continuum curvature, and not specific absorption features. We note that this gives scope for possible degeneracy to occur. This degeneracy could arise from the relation between column density, temperature, and metallicity, but also due to features such as soft excess and reflection humps. We examine the potential impact of such soft excess and reflection components in Section 5.

Table 2. Free parameter limits in the IGM model. Continuum parameters are also left free. The fixed parameters are Galactic $\log(N_{\rm HX}/{\rm cm}^{-2})$, the IGM slab redshift at half the QSO redshift, and the QSO host CGM $\log(N_{\rm HX}/{\rm cm}^{-2})$, temperature, and metallicity.

IGM parameter	Range in XSPEC models
Column density	$19 \leq \log(N_{\rm HX}/{\rm cm}^{-2}) \leq 23$
Temperature	$4 \leq \log(T/{\rm K}) \leq 8$
Metallicity	$-4 \leq [X/{\rm H}] \leq -0.7$

Our IGM model assumes a plane-parallel uniform slab geometry in ionization and thermal equilibrium to model the IGM LOS (e.g. Savage et al. 2014; Khabibullin & Churazov 2019; Lehner et al. 2019). As an approximation of the full LOS IGM absorption, in a homogeneous medium, this slab is located at half the QSO redshift. In Section 4.2, we explore the impact of this slab redshift assumption on the resulting $N_{\rm HXIGM}$.

We use the same IGM parameter ranges as D21a and D21b for density, temperature, and metallicity as summarized in Table 2. The metallicity range is broad enough to cover the most diffuse low metallicity IGM regions, to the higher metallicity warm-hot IGM (WHIM) based on e.g. Schaye et al. (2003), Aguirre et al. (2008), Danforth et al. (2016), and Pratt et al. (2018).

Our model components are shown in the example in Fig. 1 for the LOS absorption to a QSO at $z = 3$. We show the model components separately using a log-parabolic power law for each line, as well as the full combined model: CIE IGM absorption (grey) for a slab at $z = 1.5$ $\log(N_{\rm HXIGM}/{\rm cm}^{-2}) = 22.00$, $Z = 0.05$ Z⊙, and $\log(T/{\rm K}) = 6.00$ for a slab at $z = 1.5$; $\log(N_{\rm HX}/{\rm cm}^{-2}) = 20$ for our Galaxy (red); $\log(N_{\rm HX}/{\rm cm}^{-2}) = 20$ with $Z = 0.1$ Z⊙ and $\log(T/{\rm K}) = 6.00$ for the QSO host CGM (blue) at $z = 3$. The full combined model is the light blue line. The absorption lines are clearly visible in the model example, but these features would not be detected in a real spectrum due to instrument limitations and redshift smearing.

Substantial absorption by intervening neutral absorbers with $\log(N_{\rm H\,I}/{\rm cm}^{-2}) > 21.00$ is rare in QSO LOS, and insufficient to account for the observed spectral curvature unless there are several intervening DLA or a galaxy (e.g. Elvis et al. 1994a; Cappi et al. 1997; Fabian et al. 2001; Page et al. 2005). Accordingly, we omit absorption contribution from any such objects. In Section 5, we will examine all known DLA and intervening galaxies on the QSO LOS to see if they could account for any curvature in the sample spectra.

The full XSPEC models based on the above components are therefore:

TBABS(Galaxy z=0) * HOTABS(IGM slab at QSO z/2) * HOTABS(host CGM z = zQSO) * PO

Downloaded from https://academic.oup.com/mnras/article/513/1/822/6553838 by Durham University user on 28 June 2022

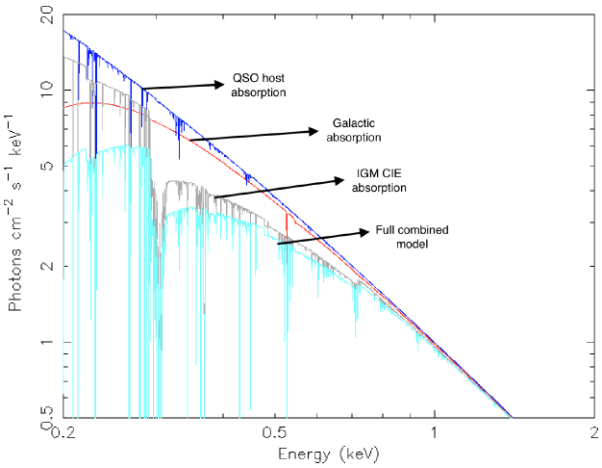

Figure 1. Model components for the LOS absorption to a QSO at $z = 3$, in the energy range 0.2–3 keV. Each component is shown separately combined with a log-parabolic power law, as well as the full combined model: IGM CIE absorption (grey) of a slab at $z = 1.5$ $\log(N_{\rm HXIGM}/{\rm cm}^{-2}) = 22.00$, $Z = 0.05$ Z$\odot$, and $\log(T/{\rm K}) = 6.00$; $\log(N_{\rm HX}/{\rm cm}^{-2}) = 20$ for our Galaxy (red); $\log(N_{\rm HX}/{\rm cm}^{-2}) = 20$ with $Z = 0.1$ Z$\odot$ and $\log(T/{\rm K}) = 6.00$ for the QSO host CGM at $z = 3$ (blue). The full combined model is the light blue line.

or

TBABS(Galaxy z=0) * HOTABS(IGM slab at QSO z/2) * HOTABS(host CGM z = zQSO) * LOGPAR

4 QSO SPECTRAL ANALYSIS RESULTS

In this section, we discuss the result of using a log-parabolic power law compared to the more commonly used simple power law for the QSO intrinsic continuum in Section 4.1. We give the IGM property results for the full sample using the CIE absorption model in Section 4.2. All spectral fits include Galactic and QSO host CGM absorption as described in Section 3.

4.1 Spectra fits using alternative continuum models

In nearly all of the sample, the Cstat fit improved using the log-parabolic power law with 60 per cent showing a significant improvement based on the criteria ΔCstat > 2.71. Accordingly, in fitting the QSO sample with the full CIE model, we used only a log-parabolic power law for consistency.

4.2 Results for IGM parameters using the CIE model

Table 3 gives the results for $\log(N_{\rm HX})$, temperature, and metallicity using the CIE IGM model component for our full QSO sample. These IGM parameters, as well as the power-law parameters were left free to vary. The error bars are with a 90 per cent confidence interval. The green line in the plots of $N_{\rm HX}$ and redshift (Figs 2 and 10), is the simple model of the mean IGM hydrogen density (equation 1) based on D20, D21a, D21b, and references therein (e.g. Starling et al. 2013; Shull & Danforth 2018):

$$N_{\rm HXIGM} = \frac{n_0 c}{H_0} \int_0^z \frac{(1+z)^2 {\rm d}z}{[\Omega_M (1+z)^3 + \Omega_\Lambda]^{\frac{1}{2}}} \quad (1)$$

where n_0 is the hydrogen density at $z = 0$, taken as 1.7×10^{-7} cm^{-3} (Behar et al. 2011). We used our results for $N_{\rm HXIGM}$ and actual redshift for the QSOs to get their equivalent n_0 which are derived by rearranging equation (1) to give n_0. We then took the mean of n_0 for our full sample and calculated the standard error.

In Fig. 2, the $N_{\rm HXIGM}$ versus redshift for the full QSO sample scales as $(1+z)^{1.5 \pm 0.2}$, reduced $\chi^2 = 0.58$ (approximated χ^2 given the uncertainties are uneven). For the RQQ dominating at redshift $z < 2$, the redshift scaling is $(1+z)^{1.9 \pm 0.3}$, while the RLQ dominating at $z > 2$ scale as $(1+z)^{1.2 \pm 0.3}$. This scaling of $N_{\rm HXIGM}$ is very similar to the simple IGM model curve (reduced $\chi^2 = 1.78$), subject to error bars i.e. it is what is expected for a diffuse IGM. The sample includes QSOs with redshift $z = 0.114$, so a linear χ^2 fit is only an approximation for the curve. The mean hydrogen density based on equation (1) for the QSO sample is $n_0 = (2.8 \pm 0.3) \times 10^{-7}$ cm^{-3} at $z = 0$, compared to 1.7×10^{-7} cm^{-3} assumed for the simple IGM model. A subsample of QSOs with $z > 1.6$, similar to the GRB sample in D21a, gives $n_0 = (2.1 \pm 0.3) \times 10^{-7}$ cm^{-3}.

Most X-ray absorption occurs below 2 keV in the rest frame. Given we are using observed 0.3–10 keV spectra, for higher redshift QSOs, the slab location assumption results in lower keV absorbing ions being redshifted out of the observed spectral range. Placing the slab at less than half the QSO redshift may better trace the low keV X-ray absorption. However, it would not reflect the impact on the observed cross-section which scales approximately as $E^{-2.5}$, and therefore for redshifted absorbers with a fixed observed energy window, the cross-section scales as $\sim(1+z)^{-2.5}$. To show the impact of placing the slab at different redshifts, other than the model location of half the QSO redshift, we used QSO 143023.73+420436.5 which is located at $z = 4.71$ as an example. We fitted the spectrum moving the IGM slab from $z = 0$ to 4.71, freezing $\log(T/{\rm K}) = 6$ and $[X/{\rm H}] = -1$. As can be seen in Fig. 3, the $N_{\rm HXIGM}$ is not substantially affected by the choice of redshift location, apart from at $z = 0$ which would not reflect any IGM absorption. The uncertainties are smaller as there are less free parameters than the full free model.

There is a broad range in the temperature across the redshift range for the QSO sample $4.9 < \log(T/{\rm K}) < 8.0$, with most having large error bars in Fig. 4. The mean temperature for the full QSO sample is $\log(T/{\rm K}) = 6.5 \pm 0.1$. It is notable that very few of the QSOs have error bars that go below $\log(T/{\rm K}) < 5.0$ even though we allow the temperature parameter to vary down to $\log(T/{\rm K}) = 4.0$. A number of the QSOs have best-fitting temperatures close to the high or low parameter range limits, indicating that temperatures are not well determined.

No relation between temperature and redshift is apparent. The IGM LOS may include a cooler photoionized gas contributing to the absorption which is not included in this CIE model. The fits are not representative of any individual absorber temperature, but instead represent the integrated LOS.

There is no apparent relation between $[X/{\rm H}]$ and redshift in Fig. 5. The mean metallicity is $[X/{\rm H}] = -1.31 \pm 0.07$ (0.05 Z$\odot$) and ranges from approximately $[X/{\rm H}] = -0.8$ (0.16 Z$\odot$) to $[X/{\rm H}] = -2.9$ (0.001 Z$\odot$). Most of the QSOs appear to favour metallicity in the range $-1 \leq [X/{\rm H}] \leq -2.0$, with only a small number favouring lower metallicities, generally at lower redshifts. This appears to be contrary to any expected evolution of metallicity, though our approach is based on the full LOS to the QSOs and not any particular absorber redshift.

Based on our results, the CIE model using HOTABS is plausible for modelling the warm/hot component of the IGM at all redshifts, with the caveats of using only a CIE IGM component, the slab model being representative of the full LOS, and low X-ray resolution. In particular, we note that the results are sensitive to the assumption that placing the slab at half the QSO redshift is representative of the diffuse IGM.

Downloaded from https://academic.oup.com/mnras/article/513/1/822/6553838 by Durham University user on 28 June 2022

Table 3. Full IGM model fitting results for the SDSS-DR14 and 4*XMM–Newton*-DR9 cross-correlation QSO sample. For each QSO, the columns give the name, redshift, IGM parameters ($N_{\rm HXIGM}$, [X/H], and temperature), continuum log-parabolic power law (PO), curvature parameter β, and Cstat/degrees of freedom (dof).

QSO	z	$\log\left(\frac{N_{\rm HXIGM}}{\rm cm^{-2}}\right)$	[X/H]	$\log\left(\frac{T}{\rm K}\right)$	PO	β	Cstat/dof
J142952+544717	6.18	$22.28^{+0.30}_{-0.24}$	$-1.48^{+0.46}_{-0.44}$	$5.72^{+0.78}_{-0.39}$	$2.67^{+0.25}_{-0.26}$	$-0.96^{+1.42}_{-0.02}$	483.20/1940
022112.62−034252.2	5.01	$22.60^{+0.04}_{-1.03}$	$-1.14^{+0.11}_{-0.75}$	$7.91^{+0.04}_{-2.67}$	$2.13^{+0.37}_{-0.42}$	$0.94^{+0.00}_{-1.65}$	110.04/1940
001115.23+144601.8	4.96	$22.47^{+0.12}_{-1.01}$	$-1.06^{+0.17}_{-1.34}$	$7.98^{+0.00}_{-2.78}$	$1.51^{+0.88}_{-0.01}$	$0.64^{+0.22}_{-0.29}$	639.73/1940
143023.73+420436.5	4.71	$22.20^{+0.40}_{-0.31}$	$-1.75^{+0.90}_{-1.65}$	$5.00^{+0.40}_{-0.33}$	$1.84^{+0.14}_{-0.06}$	$-0.22^{+0.11}_{-0.14}$	1604.58/1940
223953.6−055220.0	4.56	$22.58^{+0.08}_{-0.61}$	$-0.84^{+0.12}_{-0.95}$	$7.98^{+0.01}_{-1.48}$	$1.83^{+0.63}_{-0.23}$	$-0.22^{+1.42}_{-0.02}$	483.20/1940
151002.93+570243.3	4.31	$22.19^{+0.25}_{-0.54}$	$-1.42^{+0.42}_{-1.10}$	$5.96^{+0.44}_{-1.71}$	$2.00^{+0.23}_{-0.31}$	$-0.59^{+0.41}_{-0.30}$	621.21/1940
133529.45+410125.9	4.26	$22.48^{+0.01}_{-1.37}$	$-0.93^{+0.18}_{-1.38}$	$7.54^{+0.12}_{-1.64}$	$1.61^{+0.62}_{-0.12}$	$0.15^{+0.28}_{-0.76}$	334.92/1940
132611.84+074358.3	4.12	$22.16^{+0.10}_{-1.26}$	$-1.30^{+0.54}_{-1.00}$	$6.88^{+1.04}_{-2.39}$	$2.06^{+0.32}_{-0.21}$	$-0.34^{+0.47}_{-0.34}$	352.29/1940
163950.52+434003.7	3.99	$22.55^{+0.03}_{-1.47}$	$-1.12^{+0.39}_{-0.93}$	$6.96^{+0.95}_{-2.08}$	$1.75^{+0.35}_{-0.06}$	$-0.09^{+0.45}_{-0.03}$	436.57/1940
021429.29−051744.8	3.98	$22.46^{+0.02}_{-1.42}$	$-1.62^{+0.87}_{-0.60}$	$7.36^{+0.57}_{-2.23}$	$2.19^{+0.18}_{-0.15}$	$-0.25^{+0.47}_{-0.38}$	516.95/1940
133223.26+503431.3	3.81	$22.34^{+0.19}_{-0.66}$	$-1.48^{+0.39}_{-0.26}$	$6.62^{+1.21}_{-0.71}$	$2.17^{+0.19}_{-0.78}$	$-0.50^{+1.00}_{-0.50}$	240.41/1940
200324.1−325144.0	3.78	$22.32^{+0.10}_{-1.04}$	$-1.32^{+0.59}_{-0.78}$	$6.90^{+1.04}_{-1.84}$	$1.94^{+0.06}_{-0.33}$	$-0.08^{+0.36}_{-0.07}$	757.08/1940
200324.1–135245.1	3.77	$22.25^{+0.18}_{-0.88}$	$-1.03^{+0.30}_{-1.19}$	$7.02^{+0.90}_{-1.30}$	$1.80^{+0.06}_{-0.18}$	$0.05^{+0.19}_{-0.08}$	735.85/1940
122135.6+280614.0	3.31	$22.45^{+0.04}_{-1.15}$	$-1.15^{+0.43}_{-0.77}$	$7.95^{+0.02}_{-2.70}$	$1.26^{+0.21}_{-0.07}$	$0.18^{+0.16}_{-0.18}$	843.48/1940
042214.8−384453.0	3.11	$22.31^{+0.13}_{-0.06}$	$-1.09^{+0.37}_{-0.63}$	$7.00^{+0.46}_{-1.20}$	$2.17^{+0.20}_{-0.32}$	$-0.12^{+0.37}_{-0.32}$	527.00/1940
083910.89+200207.3	3.03	$22.05^{+0.34}_{-1.27}$	$-1.00^{+0.28}_{-1.00}$	$6.40^{+1.45}_{-1.92}$	$1.60^{+0.03}_{-0.38}$	$-0.32^{+0.39}_{-0.06}$	1048.72/1940
111038.64+483115.6	2.96	$22.32^{+0.09}_{-1.11}$	$-1.31^{+0.59}_{-0.61}$	$6.65^{+1.18}_{-0.69}$	$2.50^{+0.11}_{-0.61}$	$-0.45^{+0.70}_{-0.27}$	333.61/1940
122307.52+103448.2	2.75	$22.22^{+0.05}_{-0.75}$	$-1.34^{+0.58}_{-0.89}$	$6.28^{+1.61}_{-0.68}$	$2.69^{+0.18}_{-0.90}$	$-0.79^{+1.27}_{-0.07}$	261.18/1940
115005.36+013850.7	2.33	$22.15^{+0.17}_{-0.45}$	$-1.04^{+0.29}_{-0.82}$	$6.76^{+1.10}_{-1.65}$	$3.58^{+0.39}_{-0.50}$	$-2.02^{+1.07}_{-0.65}$	316.75/1940
121423.02+024252.8	2.22	$21.98^{+0.37}_{-0.58}$	$-2.70^{+1.13}_{-0.30}$	$4.98^{+0.29}_{-0.13}$	$2.09^{+0.18}_{-0.14}$	$-0.48^{+0.21}_{-0.28}$	1256.46/1940
112338.14+052038.5	2.18	$22.27^{+0.08}_{-0.91}$	$-1.30^{+0.38}_{-0.70}$	$6.96^{+0.70}_{-1.09}$	$2.09^{+0.46}_{-0.38}$	$-0.27^{+0.48}_{-0.52}$	415.64/1940
123527.36+392824.0	2.16	$22.07^{+0.05}_{-1.22}$	$-1.13^{+0.40}_{-0.76}$	$5.38^{+0.94}_{-1.16}$	$2.67^{+0.21}_{-0.69}$	$-0.91^{+1.03}_{-0.24}$	270.33/1940
134740.99+581242.2	2.05	$22.16^{+0.14}_{-0.98}$	$-1.19^{+0.41}_{-0.73}$	$6.63^{+1.17}_{-0.38}$	$2.17^{+0.26}_{-0.21}$	$-0.23^{+0.16}_{-0.38}$	638.71/1940
095834.04+024427.1	1.89	$22.38^{+0.04}_{-1.21}$	$-1.54^{+0.76}_{-0.51}$	$7.11^{+0.73}_{-1.54}$	$2.27^{+0.33}_{-0.10}$	$-0.52^{+0.22}_{-0.47}$	500.15/1940
093359.34+551550.7	1.86	$22.04^{+0.17}_{-0.53}$	$-1.24^{+0.52}_{-0.43}$	$5.30^{+0.90}_{-0.45}$	$1.29^{+0.22}_{-0.07}$	$-1.00^{+0.00}_{-0.25}$	659.00 /1940
133526.73+405957.5	1.77	$22.45^{+0.08}_{-1.34}$	$-1.17^{+0.45}_{-0.79}$	$7.84^{+0.10}_{-1.42}$	$1.58^{+0.22}_{-0.12}$	$0.11^{+0.33}_{-0.28}$	303.33/1940
100434.91+411242.8	1.74	$22.46^{+0.10}_{-0.91}$	$-0.80^{+0.07}_{-1.60}$	$7.88^{+0.10}_{-1.42}$	$1.81^{+0.06}_{-0.09}$	$-0.07^{+0.21}_{-0.07}$	1002.61/1940
104039.54+061521.5	1.58	$22.31^{+0.02}_{-1.36}$	$-1.30^{+0.44}_{-0.40}$	$7.18^{+0.66}_{-1.62}$	$2.06^{+0.42}_{-0.12}$	$0.21^{+0.33}_{-0.73}$	360.88/1940
083205.95+524359.3	1.57	$22.28^{+0.16}_{-0.95}$	$-1.44^{+0.70}_{-1.56}$	$6.89^{+0.95}_{-1.37}$	$2.39^{+0.33}_{-0.26}$	$-0.28^{+0.49}_{-0.53}$	444.36/1940
112320.73+013747.4	1.47	$22.13^{+0.02}_{-1.02}$	$-1.23^{+0.02}_{-0.73}$	$6.52^{+0.24}_{-0.70}$	$1.08^{+0.24}_{-0.14}$	$1.12^{+0.51}_{-0.03}$	639.3/1940
091301.03+525928.9	1.38	$21.93^{+0.47}_{-1.93}$	$-0.90^{+0.18}_{-1.80}$	$7.10^{+0.82}_{-1.55}$	$2.02^{+0.09}_{-0.07}$	$-0.44^{+0.15}_{-0.17}$	595.67/1940
121426.52+140258.9	1.28	$22.41^{+0.10}_{-1.11}$	$-0.90^{+0.18}_{-1.25}$	$7.79^{+0.16}_{-0.90}$	$1.89^{+0.06}_{-0.06}$	$-0.21^{+0.17}_{-0.09}$	805.58/1940
105316.75+573550.8	1.21	$22.06^{+0.25}_{-1.06}$	$-1.20^{+0.44}_{-1.20}$	$7.00^{+0.94}_{-1.13}$	$2.19^{+0.06}_{-0.12}$	$-0.32^{+0.22}_{-0.20}$	588.84/1940
085808.91+274522.7	1.09	$21.52^{+0.84}_{-0.44}$	$-2.30^{+1.51}_{-0.70}$	$5.06^{+2.87}_{-0.04}$	$2.39^{+0.05}_{-0.17}$	$-0.33^{+0.34}_{-0.05}$	655.53/1940
095857.34+021314.5	1.02	$21.04^{+1..34}_{-0.44}$	$-1.07^{+0.33}_{-1.07}$	$5.58^{+2.35}_{-0.34}$	$2.04^{+0.13}_{-0.20}$	$-0.19^{+0.29}_{-0.19}$	553.17/1940
125849.83−014303.3	0.97	$22.08^{+0.45}_{-0.66}$	$-1.10^{+0.35}_{-0.90}$	$7.04^{+0.39}_{-0.20}$	$2.29^{+0.69}_{-0.06}$	$-0.23^{+0.10}_{-0.65}$	904.00/1940
082257.55+404149.7	0.87	$21.32^{+0.86}_{-0.15}$	$-0.91^{+0.17}_{-1.49}$	$5.04^{+2.84}_{-0.0}$	$2.51^{+0.07}_{-0.45}$	$-0.90^{+0.72}_{-0.05}$	365.24/1940
150431.30+474151.2	0.82	$21.71^{+0.74}_{-0.53}$	$-1.62^{+0.90}_{-0.48}$	$5.59^{+2.37}_{-0.00}$	$2.15^{+0.73}_{-0.19}$	$-0.11^{+0.44}_{-0.66}$	407.23/1940
111606.97+423645.4	0.67	$21.66^{+0.51}_{-0.96}$	$-1.13^{+0.36}_{-0.83}$	$5.84^{+1.90}_{-0.22}$	$1.94^{+0.06}_{-0.23}$	$-0.26^{+0.28}_{-0.08}$	680.82 /1940
130028.53+283010.1	0.65	$21.36^{+0.97}_{-0.89}$	$-1.00^{+0.27}_{-1.99}$	$6.88^{+1.07}_{-0.82}$	$1.96^{+0.04}_{-0.04}$	$-0.06^{+0.08}_{-0.10}$	971.87/1940
111135.76+482945.3	0.56	$20.85^{+1.35}_{-0.54}$	$-0.99^{+0.23}_{-1.17}$	$7.83^{+0.04}_{-2.44}$	$2.26^{+0.11}_{-0.04}$	$-0.12^{+0.13}_{-0.17}$	633.63/1940
091029.03+542719.0	0.53	$21.34^{+0.98}_{-0.30}$	$-1.72^{+0.96}_{-0.68}$	$5.07^{+2.80}_{-0.03}$	$2.61^{+0.08}_{-0.25}$	$-0.68^{+0.55}_{-0.04}$	599.13/1940
105224.94+441505.2	0.44	$21.18^{+1.09}_{-0.48}$	$-0.88^{+0.16}_{-1.08}$	$5.99^{+1.88}_{-0.49}$	$2.48^{+0.14}_{-0.19}$	$-0.40^{+0.44}_{-0.26}$	419.56/1940
223607.68+134355.3	0.33	$21.86^{+0.37}_{-1.87}$	$-0.84^{+0.12}_{-1.21}$	$6.89^{+0.95}_{-1.84}$	$2.69^{+0.19}_{-0.03}$	$-0.20^{+0.12}_{-0.45}$	510.23/1940
144645.93+403505.7	0.27	$20.60^{+0.98}_{-0.90}$	$-1.85^{+0.30}_{-1.85}$	$5.03^{+0.09}_{-0.01}$	$2.98^{+0.02}_{-0.10}$	$-0.71^{+0.19}_{-0.04}$	885.25/1940
123054.11+110011.2	0.24	$21.15^{+0.73}_{-0.85}$	$-2.52^{+1.03}_{-0.48}$	$5.07^{+0.13}_{-0.04}$	$2.57^{+0.17}_{-0.07}$	$-0.59^{+0.14}_{-0.07}$	679.62/1940
103059.09+310255.8	0.18	$20.90^{+1.06}_{-0.43}$	$-2.80^{+0.82}_{-0.16}$	$5.06^{+0.14}_{-0.01}$	$2.28^{+0.05}_{-0.06}$	$-0.53^{+0.08}_{-0.06}$	1514.88/1940
141700.81+445606.3	0.11	$21.00^{+0.66}_{-1.00}$	$-2.85^{+0.87}_{-0.15}$	$5.09^{+0.06}_{-0.03}$	$2.70^{+0.04}_{-0.07}$	$-0.57^{+0.10}_{-0.07}$	1216.11/1940

Downloaded from https://academic.oup.com/mnras/article/513/1/822/6553838 by Durham University user on 28 June 2022

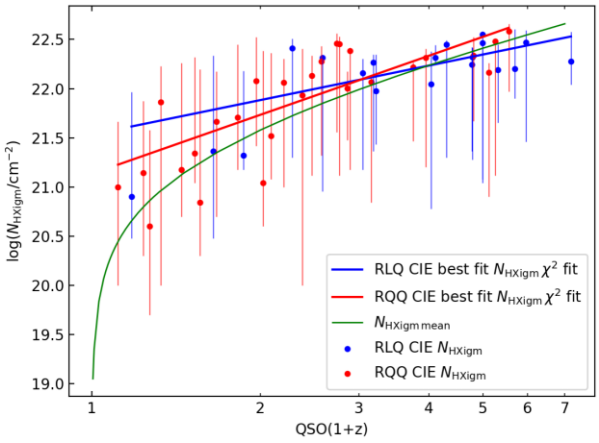

Figure 2. Results for the IGM N_{HX} parameter versus redshift using the CIE (HOTABS) model. RLQ are blue and RQQ are red. The error bars are with a 90 per cent confidence interval. The green line is the simple IGM model (see equation 1).

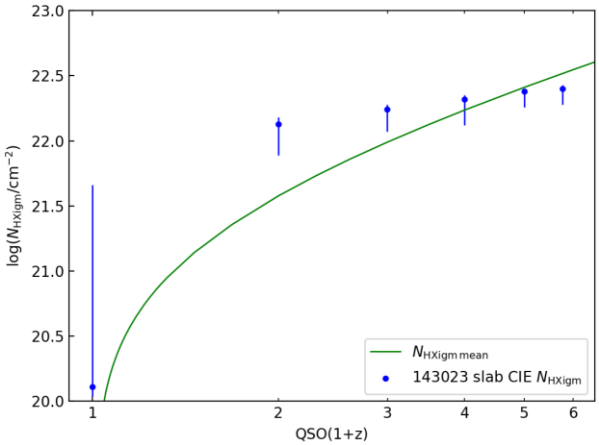

Figure 3. The impact on N_{HXIGM} for 143023.73+420436.5 by moving the IGM slab from $z = 0$ to 4.71, freezing $\log(T/K) = 6$ and $[X/H] = -1$. The green line is the simple IGM model.

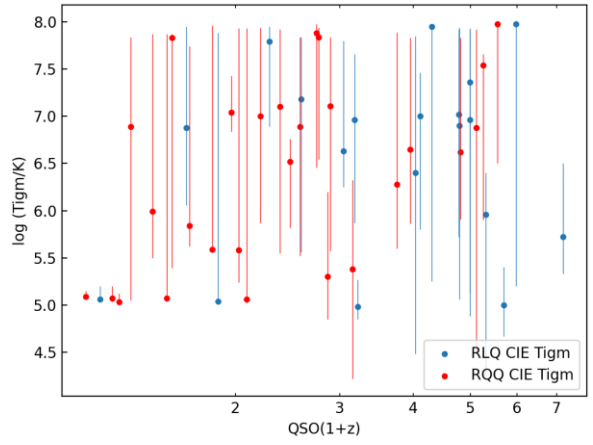

Figure 4. Results for the $\log(T/K)$ IGM versus redshift using the CIE model. RLQ are blue and RQQ are red. The error bars are with a 90 per cent confidence interval. The fit was too poor for a χ^2 curve due to the large scatter.

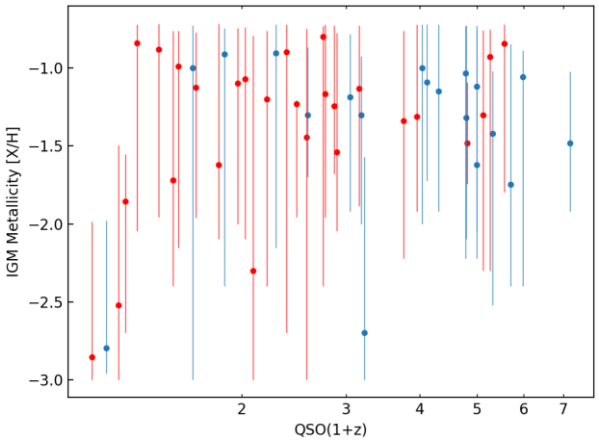

Figure 5. IGM metallicity versus redshift using the CIE model. RLQ are blue and RQQ are red. The error bars are with a 90 per cent confidence interval. We do not include a χ^2 curve in the plot as the fit was poor due to the large scatter.

In all fits, the Cstat was improved by using the IGM component. Further, 73 per cent show a significant improvement with the IGM component added based on the criteria ΔCstat > 6.25 for three interesting parameters. The average Cstat improvement for the full sample per free IGM parameter was 8.25. Our metallicity and temperature ranges, and mean results are consistent with simulations for a warm/hot phase, with the caveat that we model the continuum curvature and not specific absorption features so there is scope for degeneracy in the three free IGM parameters.

In Section 5, we test the robustness of our results.

5 TESTS FOR ROBUSTNESS OF IGM PARAMETER RESULTS

AGN are generally known to have a Compton hump at higher energies. Similarly, at lower energies, a soft excess is sometimes observable in AGN spectra, whose cause is still debated. Both, or either, of these features, if present in a QSO spectrum, may affect any absorption feature of the IGM. N_{HXIGM} may be degenerate with continuum slope and intrinsic curvature. Further, QSO spectra have very large differences in total counts and count rates which could have an impact on or be linked to spectral curvature. There is a large range in luminosity of QSOs and this may be a source of the apparent N_{HXIGM} redshift relation. Finally, we look for absorbers in UV and lensing galaxies to investigate their possible contribution to the column density.

5.1 IGM column density and intrinsic power-law index

There is scope for degeneracy between N_{HXIGM} and spectral slope and curvature. To measure the unabsorbed continuum slope, we used a log-parabolic power law only. RQQ are dominant at $z < 2$, and typically have a higher power index than RLQ which dominate above $z > 2$ (e.g. Reeves & Turner 2000; Page et al. 2005; Scott et al. 2011), which is consistent with our results. Fig. 6 (left-hand panel) does not show a strong relation between the QSO power-law index and redshift, other than that expected from the redshift spread of RQQ and RLQ. There have been many studies over the years examining possible evolution or relations of QSO continua with redshift. The results consistently have been that there is no such evolution or relation (e.g. Reeves & Turner 2000; Page et al. 2005; Grupe et al.

Downloaded from https://academic.oup.com/mnras/article/513/1/822/6553838 by Durham University user on 28 June 2022

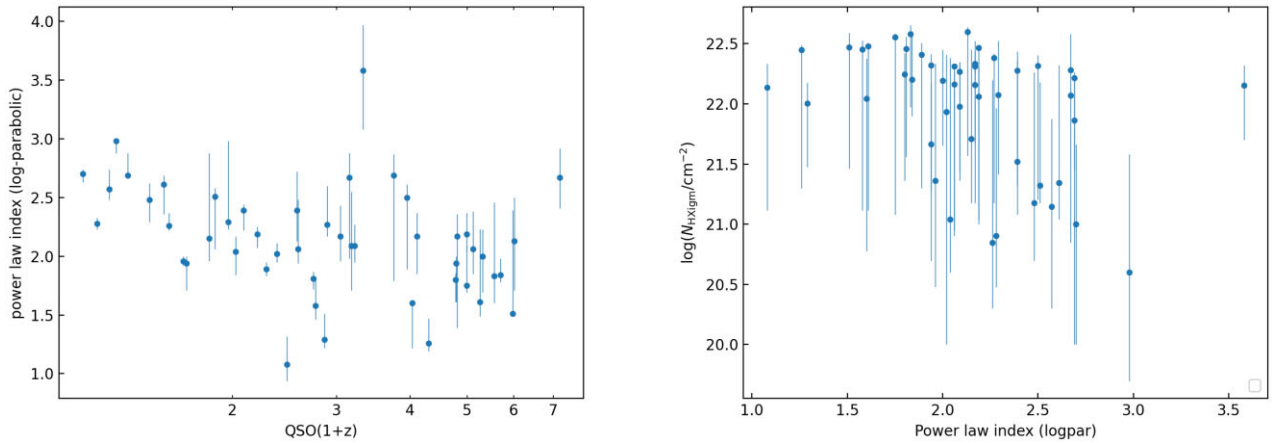

Figure 6. Testing for a possible relation between *N*HXIGM and the QSO intrinsic power-law index (log-parabolic). Left-hand panel is the QSO intrinsic power-law index versus redshift. There is no apparent strong relation between the power law and redshift, other than that due to the dominance of RQQ below $z < 2$ which are known to have a higher power-law index than RLQ. The right-hand panel is *N*HXIGM and the QSO intrinsic power-law index which does not show any apparent relation between the variables.

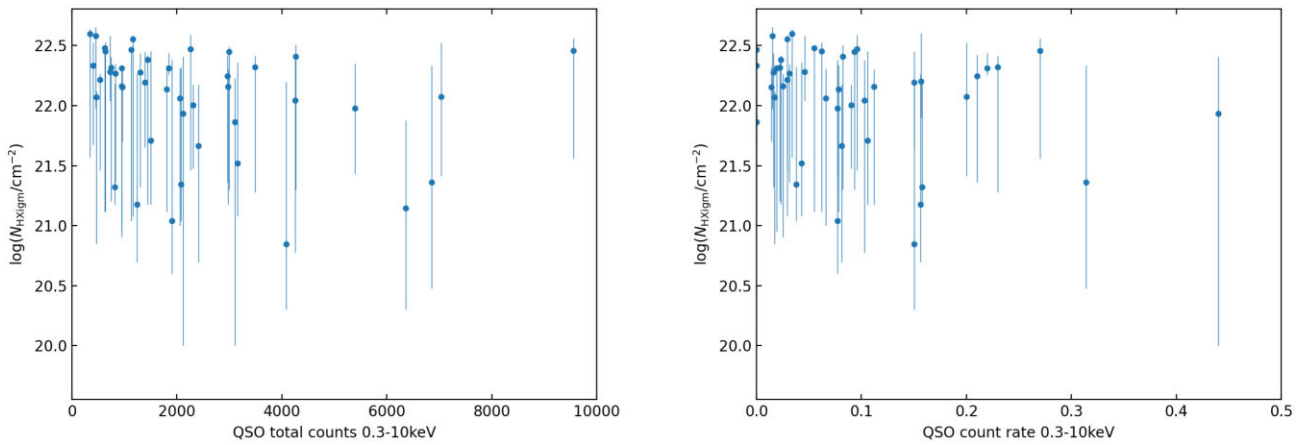

Figure 7. Left-hand panel: Testing for any relation between the QSO *N*HXIGM and total spectral counts. Right-hand panel: Testing for any relation between *N*HXIGM and spectral count rates. There is no apparent relation between the variables.

2006; Risaliti & Lusso 2019; Shehata et al. 2021). This supports the argument that the observed *N*HX redshift relation in our results is IGM related and not intrinsic to the QSO properties, as there is no apparent relation between our *N*HXIGM results and power-law index in Fig. 6 (right-hand panel).

5.2 IGM column density and spectral counts

Since the QSO spectra and therefore *N*HXIGM will be better constrained for observations with higher statistics, total counts and count rates, this may lead to a bias. We check this by looking for any relation between the index and net counts and count rates. Fig. 7 (left-hand panel) shows no relation between the QSO *N*HXIGM and total counts. There is also no apparent relation between *N*HXIGM and count rates in Fig. 7 (right-hand panel), as expected given that there is no obvious physical reason why a higher flux should be linked to column density, consistent with prior studies (e.g. Shehata et al. 2021).

5.3 IGM column density and luminosity

The majority of QSOs are RQQ with only approximately 10 per cent being RLQ, though this varies somewhat with redshift (e.g. Grupe et al. 2006). However, RQQ are mostly observed at $z < 2$. Given we are selecting the QSOs with the highest counts, and also out to the highest redshifts, there is scope for luminosity bias which may be degenerate with *N*HXIGM. In Fig. 8 (left-hand panel), we plot the SDSS-DR14 and 4*XMM–Newton*-DR9 cross-correlated catalogue with a cutoff of >1000 counts. A clear luminosity redshift relation is notable. In Fig. 8 (right-hand panel), a plot of our QSO sample with redshift shows a similar luminosity redshift relation.

In Fig. 9, we plot our QSO *N*HXIGM and luminosity. Given the luminosity bias in our sample, and the observed luminosity redshift relation in both our sample and the full SDSS-*XMM–Newton* catalogue, it is not surprising that there is also an apparent *N*HXIGM luminosity relation. This relation has been noted previously and it is not possible to determine which parameter of either luminosity or redshift, that *N*HXIGM is more closely related (Eitan & Behar 2013; Shehata et al. 2021), or whether the luminosity relationship

Downloaded from https://academic.oup.com/mnras/article/513/1/822/6553838 by Durham University user on 28 June 2022

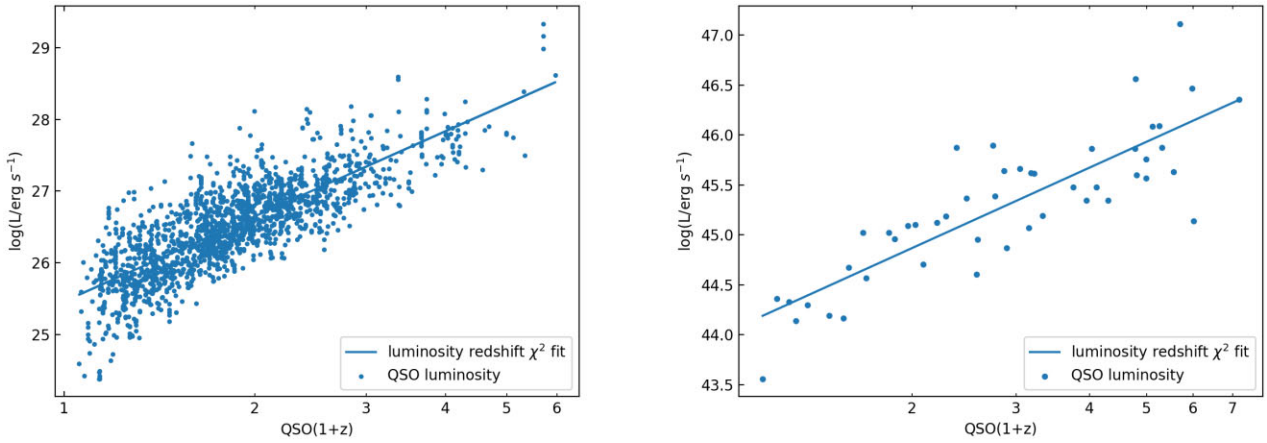

Figure 8. Left-hand panel: Monochromatic luminosity (2 keV) and redshift for the full SDSS-DR14 and 4*XMM–Newton*-DR9 with counts >1000. Right-hand panel: Our QSO sample luminosity for energy 2–10 keV and redshift.

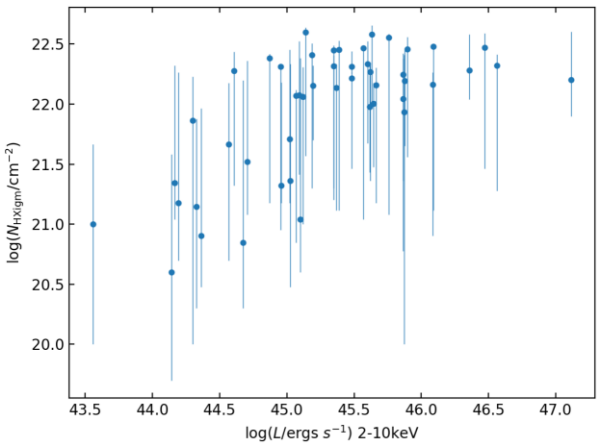

Figure 9. Testing for a possible relation between *N*HXIGM and luminosity.

is causal in any way on *N*HXIGM. The results of *N*HXIGM redshift relations for other tracers in Section 6 should help clarify this point. In that section, we note that GRBs, blazars, and QSOs all show a very similar consistent relation between *N*HXIGM and redshift supporting the argument that the rising *N*HXIGM is not caused by luminosity.

5.4 Compton reflection hump

A Compton or reflection hump feature is common in AGNs at a rest frame of 30 keV. Depending on the redshift, this could appear in the spectra observed frame between 0.3–10 keV, especially above $z > 3$. The most common model in XSPEC used for this feature is PEXRAV (Magdziarz & Zdziarski 1995), which assumes an optically thick, cold material, distributed in a slab. In our test fitting, we left the parameter R (slab scaling parameter) free, with the power law and normalization tied to continuum power law, and with the other parameters set to XSPEC default values following the conventional approach (e.g. Reeves & Turner 2000; Ricci et al. 2017). We refitted all our QSO sample with PEXRAV instead of our CIE IGM component. For most of the QSOs, the Cstat fit was worse with PEXRAV. For all QSOs with $z > 3$, the reflection parameter results were $R \ll 1$. For the small number of QSOs that had similar Cstat results as for the CIE IGM model, a visual inspection of the spectra indicated a possible Fe feature at a rest frame of 6–7 keV. When refitted with the CIE IGM component added, the IGM parameters did not change i.e. the inclusion of the relection component did not impact the result. For the two lowest redshift QSOs, the Cstat fit improved significantly with both PEXRAV and our CIE IGM model included (being ΔCstat = 11.5 and 7.7 for QSOs 103059.09+310255.8 and 141700.81+445606.3, respectively). However, again, for these two low redshift QSOs, the IGM fit parameters did not alter substantially.

Our results are consistent with previous studies for QSOs which found that the reflection component was very weak or consistent with no reflection in both RQQ and RLQ and that this was inversely related to luminosity, known as the X-ray Baldwin effect (e.g. Iwasawa & Taniguchi 1993; Reeves & Turner 2000).

5.5 Soft excess

Many AGN show a soft excess in their X-ray spectra e.g. Ricci et al. (2017) who found that over 50 per cent of their AGN showed evidence of soft excess. However, their AGN sample was restricted to $z < 0.3$. The soft excess is typically modelled as a blackbody as a simple representation, with a peak rest-frame temperature of ∼0.1 keV, and a range of $0.01 \leq kT \leq 0.3$ keV (e.g. Reeves & Turner 2000; Scott et al. 2011; Ricci et al. 2017).

We refitted all our sample with a redshifted blackbody, ZBBODY in XSPEC instead of the IGM component. None of our QSOs with $z > 0.3$ showed any evidence of a soft excess consistent with previous studies (e.g. Reeves & Turner 2000). For the four QSOs with $z < 0.3$ the inclusion of a blackbody with a simple power law, did improve the Cstat fit. For the three lowest redshift QSOs, the inclusion of the IGM component as well as a blackbody component significantly improved the fit (ΔCstat > 6.25). However, the IGM fitted parameters did not alter substantially.

5.6 Large absorbers on the LOS

To test whether DLAs could account for some of the absorption on the LOS, we reviewed the SDSS spectra[1] for evidence of DLAs and cross-checked with the new catalogue based on SDSS DR16Q (Ho, Bird & Garnett 2021). Our results for DLAs on the QSO LOS were consistent with (Prochaska & Neeleman 2018), who were investigating the average number of DLAs intersected by a LOS to

[1] http://skyserver.sdss.org/dr16/en/tools/explore/

Downloaded from https://academic.oup.com/mnras/article/513/1/822/6553838 by Durham University user on 28 June 2022

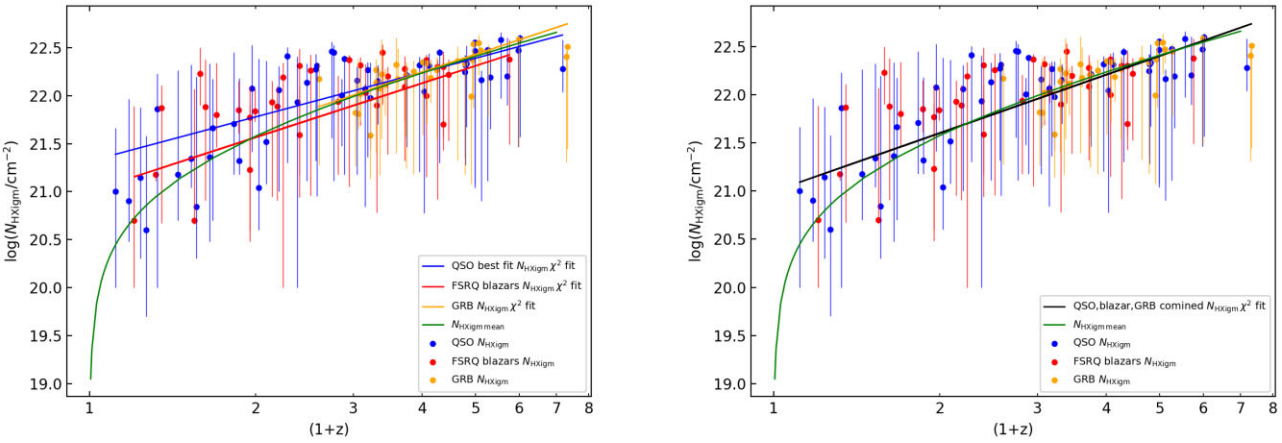

Figure 10. *N*HXIGM versus redshift for the full QSO sample (blue) combined with the FSRQ blazars from D21b (red) and the GRBs (yellow) from D21a. In the left-hand panel, each tracer group has its own χ^2 line fit. The green line is the simple IGM model based on a mean IGM density of $n_0 = 1.7 \times 10^{-7}$ cm^{-3} at $z = 0$ (see equation 1). In the right-hand panel, the χ^2 line fit is for the entire tracer samples.

a source at redshift out to $z \sim 5$. We found one QSO with a DLA between $2 \leq z \leq 3$, and eight QSOs with DLAs between $3 \leq z \leq 5$. None had more than two DLAs on a particular QSO LOS. All of these QSOs in our sample, which showed DLAs from the SDSS, had $\log(N\text{HXIGM/cm}^{-2}) > 22$, and therefore the DLA contribution would be insignificant to the column.

Intervening lensing galaxies on the QSO LOS have been observed over the years. We reviewed literature and identified two of our sample QSOs with confirmed intervening lenses, 042214.8−384453.0 and 100434.91+411242.8. The neutral column through these lensing galaxies was estimated as $\log(N_{\rm H\,I}/\text{cm}^{-2}) < 20$, two orders of magnitude lower than our measured *N*HXIGM (Carswell et al. 1996; Chen et al. 2012).

In conclusion, our robustness tests have demonstrated that, with the possible exception of luminosity, we have ruled out alternative explanations for the observed *N*HXIGM redshift relation including reflection hump, soft excess, power-law index, and spectral counts, intervening DLA and lensing galaxies. We note that the use of a log-parabolic power law may be showing an improved fit over a simple power law in all our QSO sample as either an intrinsic continuum feature, or a slight signature of the reflection hump and soft excess. As for luminosity, in the next section we compare our QSO results with our previous GRB and blazar results to see if there are consistencies which would help rule out the luminosity degeneracy.

6 COMBINED QSO, GRB, AND BLAZAR SAMPLE ANALYSIS

In this section, we combine the results from our full series of papers on using different tracers to probe the IGM column density, temperature, and metallicity. Given the differences in the tracer host environment, we adopted different approaches in estimating any host absorption. In D20 and D21a, we assumed that the GRB host intrinsic *N*HX was equal to the ionization-corrected intrinsic neutral column measured in UV, using more realistic host galaxy metallicities, dust corrected where available. In D21b, using blazars, we assumed no host absorption, relying on the fact that blazars are thought to have negligible X-ray absorption on the LOS within the host galaxy due to the relativistic jet. Finally, in this paper using QSOs, as set out in Section 3, we assume a CGM model absorption. Apart from these differences in modelling the host absorption, all other methods and models are consistently used for the three tracers.

In Fig. 10, we plot the combined tracer samples for *N*HXIGM and redshift. In the left-hand panel, the approximated linear χ^2 fits are shown separately for each tracer. Though there are differences in the linear slopes, all three are reasonably close to the simple IGM curve. In the right-hand panel, we show the χ^2 linear fit for the combined samples. This fit is also close to the simple IGM curve. In Table 4, we give the main IGM parameter results from each tracer and in combination including the mean hydrogen density at $z = 0$, *N*HXIGM versus redshift power-law fit, mean temperature and metallicities, and the ranges.

The first IGM parameter, the mean hydrogen density at $z = 0$ is given for both the full redshift range and also for our tracers with $z > 1.6$. Our GRB sample in D21a took $N_{\rm H\,I}$ data from Tanvir et al. (2019) who had a cutoff at $z = 1.6$, as below this redshift, the observed Ly α transmission declines due to Earth's atmosphere. All of the values for n_0 are slightly higher than the simple IGM curve based on n_0 equal to 1.7×10^{-7} cm^{-3} (see Section 4). The overall mean across the three tracers for $z > 1.6$ is $2.0 \pm 0.4 \times 10^{-7}$ cm^{-3} which is consistent with the assumed density of the plotted IGM curve within the errors.

The mean CIE IGM temperature across the tracers is $\log(T/\text{K}) = 6.3 \pm 0.3$ with a full range from 4.9 to 8.0. The mean IGM metallicity across the tracers is $[X/\text{H}] = -1.5 \pm 0.1$ with a full range from −3.0 to −0.08. These values are consistent with the CIE predictions for a warm/hot IGM. There is no apparent relation of temperature with redshift.

We conclude that the consistent combined results of our samples demonstrate that the IGM is contributing to the absorption observed in the spectra, and that it is consistent with that predicted by the simple IGM model (equation 1). We caveat this conclusion noting that it is based on the assumption that the slab model, placed at half the tracer object redshift, is a reasonable representation of the LOS through the diffuse IGM.

7 DISCUSSION AND COMPARISON WITH OTHER STUDIES

Our work has found significant excess absorption (over our Galaxy and the QSO host) in QSO spectra. Excess X-ray absorption in QSOs

Downloaded from https://academic.oup.com/mnras/article/513/1/822/6553838 by Durham University user on 28 June 2022

Table 4. Summary results for the IGM parameters from the QSO, blazar, and GRB samples from D21a and D21b, and this paper. The IGM parameters include the mean hydrogen density at $z = 0$ n_0 for the full redshift range and for $z > 1.6$, a power-law fit to the *N*HXIGM versus redshift, mean temperature and metallicities, and the ranges.

Tracer	QSO	Blazar	GRB	All
		Mean hydrogen density at $z = 0$ ($\times 10^{-7}$ cm^{-3})		
Full redshift range	2.8 ± 0.3	3.2 ± 0.5	1.8 ± 0.2	
$z > 1.6$	2.1 ± 0.3	2.1 ± 0.2	1.8 ± 0.2	2.0 ± 0.4
		Power-law fit to the *N*HXIGM versus redshift		
Slope index	1.5 ± 0.2	1.8 ± 0.2	1.9 ± 0.2	2.0 ± 0.1
		Temperature (log(*T*/K))		
Mean	6.5 ± 0.1	6.1 ± 0.1	6.3 ± 0.2	6.3 ± 0.3
Range	4.9–8.0	5.0–8.0	5.0–7.1	
		Metallicity [*X*/H]		
Mean	-1.3 ± 0.1	-1.6 ± 0.0	-1.8 ± 0.1	-1.5 ± 0.1
Range	-2.85 to -0.8	-3.0 to -0.08	-1.75 to -1.0	

has been reported in earlier studies, predominantly in RLQ rather than RQQ (e.g. Elvis et al. 1994a; Reeves & Turner 2000; Page et al. 2005). Initial possible explanations included the absorption being related to the jet, which was thought to be responsible for the Doppler boosting of the X-ray continuum (e.g. Reeves & Turner 2000). Most of these studies found the absorption tended to increase with QSO redshift. This would not support the jet absorption theory as the QSO jet luminosity was not found to increase with redshift (Scott et al. 2011). Eitan & Behar (2013) found that the optical depth increased with redshift for a sample of QSOs and GRBs, scaling as $(1 + z)^{2.2 \pm 0.6}$. This is very close to our combined tracer result for *N*HXIGM of $(1 + z)^{2.0 \pm 0.1}$. Eitan & Behar (2013) postulated that their result could be explained by an ionized and clumpy IGM at $z < 2$, and a diffuse, cold IGM at higher redshift. This scenario was improved on by Starling et al. (2013), who used a warm-hot absorber scenario for the IGM. Starling et al. (2013) concluded that their WHIM scenario could account for most of their estimated X-ray column density for GRB at $z > 3$ for IGM parameters $\log(T/\mathrm{K}) = 5$–6 and $Z/\mathrm{Z}\odot < 0.2$. The main differences and caveats on the results of Eitan & Behar (2013) and Starling et al. (2013), are that they used the conventional assumption that all excess absorption is at the host redshift, despite dealing with IGM absorption on the LOS. Further, while Eitan & Behar (2013) measured optical depth, Starling et al. (2013) used ABSORI which was compared with HOTABS for CIE modelling by D21a. ABSORI is not self-consistent, and is limited to 10 metals fixed at solar metallicity except Fe (Done et al. 1992). D21a found HOTABS to be superior for modelling a CIE IGM.

Campana et al. (2015) examined IGM absorption to GRBs and AGN using simulations. For GRBs, they reported $\log(T/\mathrm{K}) \sim 5$–$7$ and mean metallicity $Z = 0.03$ Z$\odot$. In Section 6, we showed that our results across all our tracers, QSOs, blazars, and GRBs are consistent for the IGM parameters. Our overall mean temperature and range for the IGM are $\log(T/\mathrm{K}) = 6.5 \pm 0.1$, and $4.9 < \log(T/\mathrm{K}) < 8.0$. Our mean metallicity and range on solar units are 0.05 Z$\odot$ and 0.16 Z$\odot$ to 0.001 Z$\odot$. These values are similar to Campana et al. (2015).

Arcodia et al. (2018, hereafter A18) used a blazar sample to investigate an IGM absorption scenario. Their IGM parameter results gave an average density ($z = 0$) of $n_0 = 1.0^{+0.53}_{-0.72} \times 10^{-7}$ cm^{-3} and temperature $\log(T/\mathrm{K}) = 6.45^{+0.51}_{-2.12}$. The temperature is very close to our results. Our average density at $z = 0$ across all tracers, limiting the sample to $z > 1.6$ to accommodate the GRBs, is $n_0 = 2.0 \pm 0.40 \times 10^{-7}$ cm^{-3}. A18's n_0 is less than the conventional simple IGM model of $n_0 = 1.7 \times 10^{-7}$ cm^{-3} (see Section 4). However, we do note that in our Fig. 10, some of the highest redshift tracers show *N*HXIGM, with equivalent n_0 at $z = 0$ below the simple IGM curve assumption. A18's lower result could be explained by their use of conventional assumptions of neutral and solar absorption in the IGM and their use of an older ABSORI-based model. Alternatively, our combined results may indicate that a single uniform average density is oversimplistic across the full redshift range. The result is based on the homogeneity assumption and expansion of the Universe in the Lambda cold dark matter model. However, this does not factor in the structural changes and growth which are predicted to occur over redshift. For example, the fraction of matter in the IGM is expected to be much greater at higher redshift than lower redshift, as less matter had coalesced into galaxies and clusters (McQuinn 2016).

One of our assumptions is that of CIE. The relation between ionization state and plasma temperature explicitly assumes that the gas is in an ionization equilibrium (Richter, Paerels & Kaastra 2008). Opinions on the IGM equilibrium state have differed over the years (e.g. Branchini et al. 2009; Nicastro et al. 2018). Plasma remains overionized at any temperature in non-equilibrium versus equilibrium conditions (Gnat & Sternberg 2007). It is likely that a substantial part of the baryons in the Universe is located in low-density regions where ionization equilibrium conditions persist (McQuinn 2016). An underestimation of column density may arise due to assumed equilibrium conditions (D21a and references therein).

Generally, the fraction of RLQ to RQQ is 5−10 per cent and is possibly anticorrelated with redshift (Rusinek-Abarca & Sikora 2021 and references therein). As RLQ tend to have far greater X-ray luminosity than RQQ, they are more frequently observed at higher redshift (Worrall et al. 1987; Page et al. 2005). In our study the fraction of RLQ is ∼40 per cent reflecting the X-ray loudness bias due to our higher redshift range and choice of QSOs with high counts. However, if we look at the sample below $z < 3$ in Fig. 2 where the RQQ are dominant, and the RLQ fraction is ∼26 per cent, the redshift relation is still very clear indicating that the luminosity or high redshift RLQ bias is not driving the *N*HXIGM redshift relation.

It is possible that some additional absorption occurs in the QSO host over and above our assumed CGM amount i.e. intrinsic dust or gas in the host galaxy interstellar medium. Alternatively, absorption could occur in the intercluster medium as many QSOs are located in galaxy clusters (Elvis et al. 1994b). However, higher absorption if related to neutral gas would result in higher dust measurements which are not observed (Page et al. 2005).

Downloaded from https://academic.oup.com/mnras/article/513/1/822/6553838 by Durham University user on 28 June 2022

Significant curvature is present in the spectra of many low-redshift QSOs, below $z < 1$. This fact, or alternatively that absorption features are not observed in such low-redshift tracers has been used as an argument against IGM absorption (Watson & Jakobsson 2012 and references therein). In our QSO sample, many of the lowest redshift QSOs closely follow the simple IGM curve. It is likely that spectral curvature is due to both intrinsic factors as well as IGM absorption, with the former dominant at low redshift, and the latter becoming dominant at higher redshift.

Comparing with an alternative tracer type, Fast Radio Burst (FRB) dispersion measure (DM) is used to measure the total electron column density on the LOS to the FRB host. The conventional approach with FRBs is to fix the host DM, scaled to reflect dispersion in the rest frame of the host (e.g. Shull et al. 2017; Macquart et al. 2020). The assumption is then that all excess DM (over the host and our Galaxy) is due to the IGM, similar to our approach. This is contrary to the conventional approach with GRBs, blazars, and QSOs where the assumption is all X-ray absorption in excess of our Galaxy is at the host redshift. Using FRBs, Macquart et al. (2020) derived a median baryon fraction of $\Omega_{b,H_0} = 0.056$ (68 per cent confidence interval [0.046, 0.066]). Based on this measurement, they conclude that their results are evidence of the missing baryons being present in the ionized IGM. Our median value for the baryon fraction for all our tracers with $z > 1.6$ is $\Omega_{b,H_0} = 0.048$ (68 per cent confidence interval [0.039, 0.058]) derived from $n_0 = 2.0 \pm 0.4 \times 10^{-7}$ cm^{-3}. For our full QSO sample only, the $\Omega_{b,H_0} = 0.068$ (68 per cent confidence interval [0.061, 0.075]). These values are consistent with Macquart et al. (2020).

8 CONCLUSION

We used QSOs to probe the IGM column density, metallicity, and temperature using a CIE model for the diffuse IGM. To isolate the IGM LOS contribution to the total absorption, we assumed that the QSO host absorption is based on a fixed model of CGM absorption. We use the continuum total absorption as opposed to fitting individual absorption features as, currently, the required resolution is not available in X-ray.

We tested our results for robustness covering: a relation between column density and spectral counts; spectral slope degeneracy with column density; reflection hump and soft excess impacts; luminosity column density relation; and any impact of large absorbers known of UV studies on the LOS.

We aggregated our sample with the blazars from D21b and the GRB sample from D21a to present combined results for the IGM properties.

Our main findings and conclusions are:

(i) The results for the IGM parameters are consistent across the GRBs, blazars, and QSOs. The average results across the tracers for equivalent mean hydrogen density at $z = 0$ are $n_0 = 2.0 \pm 0.4 \times 10^{-7}$ cm^{-3} for $z > 1.6$. The combined results show similar values and correlation with redshift as the simple mean IGM density model (Fig. 10, right-hand panel). The $N_{\rm HXIGM}$ versus redshift power-law fit scales as $(1+z)^{2.0 \pm 0.1}$.

(ii) For our QSO sample in this paper, $n_0 = 2.8 \pm 0.3 \times 10^{-7}$ cm^{-3}. The $N_{\rm HXIGM}$ versus redshift power-law fit scales as $(1+z)^{1.5 \pm 0.2}$.

(iii) The mean temperature across all the tracers for the CIE IGM is $\log(T/{\rm K}) = 6.3 \pm 0.3$ with a full range from 4.9 to 8.0. The mean metallicity across the tracers for the CIE IGM is $[X/{\rm H}] = -1.5 \pm 0.1$ with a full range from -3.0 to -0.08. These values are consistent with the CIE predictions for a warm/hot IGM. There is no evidence for evolution with redshift.

(iv) The mean temperature across our QSOs only sample from this paper for the CIE IGM is $\log(T/{\rm K}) = 6.5 \pm 0.1$ with a full range from 4.9 to 8.0. The mean metallicity across the QSO sample for the CIE IGM is $[X/{\rm H}] = -1.3 \pm 0.1$ with a full range from -2.9 to -0.8. These values are also consistent with the CIE predictions for a warm/hot IGM, and there is no evidence for evolution with redshift.

(v) For the QSO sample, there is no obvious relation between $N_{\rm HXIGM}$ and the robustness tested parameters for continuum power-law index or spectral counts. Further, the possible effects of the reflection hump and soft excess were shown not to impact the results for $N_{\rm HXIGM}$, and only improved the fit for the two lowest redshift QSOs. There was insufficient evidence for DLAs or intervening lens systems on the LOS to account for the measured $N_{\rm HXIGM}$ for the QSOs. Finally, there is an apparent $N_{\rm HXIGM}$ luminosity relation due luminosity bias in our sample, which is due to our sample selection for high counts and the dominance of RLQ at $z > 3$, which are more X-ray luminous than RQQ. Both $N_{\rm HXIGM}$ and luminosity rise with redshift. However, the results for $N_{\rm HXIGM}$ are consistent across all three tracers and this would support the argument that the QSO result for $N_{\rm HXIGM}$ is not dominated or caused by luminosity.

Overall in this series of papers D20, D21a, D21b, and this paper, we have demonstrated a consistent case for strong absorption in the IGM on the LOS to three different tracer types, QSOs, blazars, and GRBs. We have taken a careful approach to isolating absorption by our Galaxy and the tracer host, by examining the differing host environment conditions known to exist for the tracer types. We have also examined the possible contribution on the LOS due to large absorbers from UV QSO studies and have subjected our results to a series of robustness tests.

As we have demonstrated that there is substantial absorption in the IGM and the mean column density is related to redshift, using the conventional assumption that all excess absorption is in the tracer host, while investigating high-redshift objects could lead to errors in deriving their properties including intrinsic absorption. Our results could also be used to test cosmological models through observations of IGM properties from these high-redshift tracers. Our estimated IGM properties will be improved by instruments such as Athena, with higher energy resolution, lower energy threshold, and larger effective areas in soft X-ray energies.

ACKNOWLEDGEMENTS

We thank Ehud Behar for a detailed and insightful review of the paper. We would like to thank E. Lusso for making available the data from the SDSS DR14 and 4*XMM–Newton*-DR9 cross-correlation data set, and E. Nardini for advice on using PEXRAV and ZBBODY for QSOs. This work made use of data supplied by *XMM–Newton*, an ESA science mission with instruments and contributions directly funded by ESA member states and NASA. SLM acknowledges support from STFC (ST/P000541/1). This project has received funding from the European Research Council (ERC) under the European Union's Horizon 2020 research and innovation programme (grant agreement no. 757535) and by Fondazione Cariplo (grant no. 2018-2329).

DATA AVAILABILITY

Data including spectra fit plots for all the QSO sample, and Markov chain Monte Carl integrated probability plots are available on request – please contact Tony Dalton. The reduced *XMM–Newton* spectral files are available by contacting Efrain Gatuzz. *XMM–Newton* EPIC spectra data are available at: http://xmm-catalog.irap.omp.eu/sources. SDSS data are available at: http://skyserver.sdss.org/dr17.

Downloaded from https://academic.oup.com/mnras/article/513/1/822/6553838 by Durham University user on 28 June 2022

REFERENCES

Aguirre A., Dow-Hygelund C., Schaye J., Theuns T., 2008, ApJ, 689, 851
Arcodia R., Campana S., Salvaterra R., Ghisellini G., 2018, A&A, 616, A170
Arnaud K., 1996, Astron. Data Anal. Softw. Syst., 101, 17
Behar E., Dado S., Dar A., Laor A., 2011, ApJ, 734, 26
Branchini E. et al., 2009, ApJ, 697, 328
Campana S., Salvaterra R., Ferrara A., Pallottini A., 2015, A&A, 575, A43
Cappi M., Matsuoka M., Comastri A., Brinkmann W., Elvis M., Palumbo G., Vignali C., 1997, ApJ, 478, 492
Carswell R. F. et al., 1996, MNRAS, 278, 506
Cash W., 1979, ApJ, 228, 939
Chen B., Dai X., Kochanek C. S., Chartas G., Blackburne J. A., Morgan C. W., 2012, ApJ, 755, 24
Crummy J., Fabian A. C., Gallo L., Ross R. R., 2006, MNRAS, 365, 1067
Dalton T., Morris S. L., 2020, MNRAS, 495, 2342
Dalton T., Morris S. L., Fumagalli M., 2021a, MNRAS, 502, 5981
Dalton T., Morris S. L., Fumagalli M., Gatuzz E., 2021b, MNRAS, 508, 1701
Danforth C. W. et al., 2016, ApJ, 817, 111
Done C., Mulchaey J., Mushotzky R., Arnaud K., 1992, ApJ, 395, 275
Done C., Davis S. W., Jin C., Blaes O., Ward M., 2012, MNRAS, 420, 1848
Eitan A., Behar E., 2013, ApJ, 774, 29
Elvis M. et al., 1994a, ApJS, 95, 1
Elvis M., Fiore F., Wilkes B., McDowell J., Bechtold J., 1994b, ApJ, 422, 60
Elvis M., Fiore F., Giommi P., Padovani P., 1998, ApJ, 492, 91
Fabian A. C., Celotti A., Iwasawa K., Ghisellini G., 2001, MNRAS, 324, 628
Fiore F., Elvis M., Giommi P., Padovani P., 1998, ApJ, 492, 79
Gierliński M., Done C., 2004, MNRAS, 349, 7
Gnat O., Sternberg A., 2007, ApJS, 168, 213
Grupe D., Mathur S., Wilkes B., Osmer P., 2006, AJ, 131, 55
Haardt F., Maraschi L., 1993, ApJ, 413, 507
Hennawi J. F. et al., 2006, ApJ, 651, 61
Hennawi J. F., Prochaska J. X., 2013, ApJ, 766, 58
Ho M. F., Bird S., Garnett R., 2021, MNRAS, 507, 704
Iwasawa K., Taniguchi Y., 1993, ApJ, 413, L15
Kalberla P. M. W., Burton W. B., Hartmann D., Arnal E. M., Bajaja E., Morras R., Pöppel W. G. L., 2005, A&A, 440, 775
Kallman T. R., Bautista M. A., Goriely S., Mendoza C., Miller J. M., Palmeri P., Quinet P., Raymond J., 2009, ApJ, 701, 865
Kellermann K. I., Sramek R., Schmidt M., Shaffer D. B., Green R., 1989, AJ, 98, 1195
Khabibullin I., Churazov E., 2019, MNRAS, 482, 4972
Lehner N., Wotta C. B., Howk J. C., O'Meara J. M., Oppenheimer B. D., Cooksey K. L., 2019, ApJ, 887, 5
Lusso E. et al., 2020, A&A, 642, A150
Macquart J. P. et al., 2020, Nature, 581, 391
McQuinn M., 2016, ARA&A, 54, 313
Magdziarz P., Zdziarski A., 1995, MNRAS, 273, 837
Medvedev P., Gilfanov M., Sazonov S., Schartel N., Sunyaev R., 2021, MNRAS, 504, 576
Mushotzky R. F., Done C., Pounds K. a., 1993, ARA&A, 31, 717
Nanni R., Vignali C., Gilli R., Moretti A., Brandt W. N., 2017, A&A, 603, A128
Nicastro F. et al., 2018, Nature, 558, 406
Page K. L., Reeves J. N., O'Brien P. T., Turner M. J., 2005, MNRAS, 364, 195
Pratt C. T., Stocke J. T., Keeney B. A., Danforth C. W., 2018, ApJ, 855, 18
Prochaska J. X., Hennawi J. F., 2009, ApJ, 690, 1558
Prochaska J. X., Neeleman M., 2018, MNRAS, 474, 318
Prochaska J. X. et al., 2013, ApJ, 2, 136
Prochaska J. X., Madau P., O'meara J. M., Fumagalli M., 2014, MNRAS, 438, 476
Reeves J. N., Turner M. J., 2000, MNRAS, 316, 234
Ricci C. et al., 2017, ApJS, 233, 17
Richter P., Paerels F. B., Kaastra J. S., 2008, Space Sci. Rev., 134, 25
Risaliti G., Lusso E., 2019, Nature Astron., 3, 272
Rusinek-Abarca K., Sikora M., 2021, ApJ, 922, 202
Salvestrini F., Risaliti G., Bisogni S., Lusso E., Vignali C., 2019, A&A, 631, 1
Savage B. D., Kim T. S., Wakker B. P., Keeney B., Shull J. M., Stocke J. T., Green J. C., 2014, ApJ, 212, 8
Schaye J., Aguirre A., Kim T., Theuns T., Rauch M., Sargent W. L. W., 2003, ApJ, 596, 768
Scott A. E., Stewart G. C., Mateos S., Alexander D. M., Hutton S., Ward M. J., 2011, MNRAS, 417, 992
Shakura N., Sunyaev R., 1973, A&A, 24, 337
Shehata S. H., Misra R., Osman A. M., Shalabiea O. M., Hayman Z. M., 2021, J. High Energy Astrophys., 31, 37
Shull J. M., Danforth C. W., 2018, ApJ, 852, L11
Shull J. M., Smith B. D., Danforth C. W., 2012, ApJ, 759, 23
Shull J. M., Danforth C. W., Tilton E. M., Moloney J., Stevans M. L., 2017, ApJ, 852, L11
Starling R. L., Willingale R., Tanvir N. R., Scott A. E., Wiersema K., O'Brien P. T., Levan A. J., Stewart G. C., 2013, MNRAS, 431, 3159
Strüder L. et al., 2001, A&A, 365, L18
Tanvir N. R. et al., 2019, MNRAS, 483, 5380
Vito F. et al., 2019, A&A, 630, A118
Wang F. et al., 2020, ApJ, 896, 23
Watson D., Jakobsson P., 2012, ApJ, 754, 89
Wilkes B. J., Elvis M., 1987, ApJ, 323, 243
Willingale R., Starling R. L., Beardmore A. P., Tanvir N. R., O'brien P. T., 2013, MNRAS, 431, 394
Wilms J., Allen A., McCray R., 2000, ApJ, 542, 914
Worrall D., Giommi P., Tananbaum H., Zamorani G., 1987, ApJ, 313, 596
York D. G. et al., 2000, AJ, 120, 1579

This paper has been typeset from a TEX/LATEX file prepared by the author.

Downloaded from https://academic.oup.com/mnras/article/513/1/822/6553838 by Durham University user on 28 June 2022